



Delft University of Technology

On Crop Growth and InSAR Closure Phases

Yuan, Yan; Kleinherenbrink, Marcel; Lopez-Dekker, Paco

DOI

[10.1109/TGRS.2024.3432396](https://doi.org/10.1109/TGRS.2024.3432396)

Publication date

2024

Document Version

Final published version

Published in

IEEE Transactions on Geoscience and Remote Sensing

Citation (APA)

Yuan, Y., Kleinherenbrink, M., & Lopez-Dekker, P. (2024). On Crop Growth and InSAR Closure Phases. *IEEE Transactions on Geoscience and Remote Sensing*, 62, Article 4411412. <https://doi.org/10.1109/TGRS.2024.3432396>

Important note

To cite this publication, please use the final published version (if applicable). Please check the document version above.

Copyright

Other than for strictly personal use, it is not permitted to download, forward or distribute the text or part of it, without the consent of the author(s) and/or copyright holder(s), unless the work is under an open content license such as Creative Commons.

Takedown policy

Please contact us and provide details if you believe this document breaches copyrights. We will remove access to the work immediately and investigate your claim.

Green Open Access added to TU Delft Institutional Repository

'You share, we take care!' - Taverne project

<https://www.openaccess.nl/en/you-share-we-take-care>

Otherwise as indicated in the copyright section: the publisher is the copyright holder of this work and the author uses the Dutch legislation to make this work public.

On Crop Growth and InSAR Closure Phases

Yan Yuan, Marcel Kleinherenbrink, and Paco López-Dekker, *Senior Member, IEEE*

Abstract—The closure phase, which is a circular summation of the phases of the three multilooked interferograms, comprises a geophysical component and phase noise. In agricultural regions of southern Spain, encompassing both open crop fields and greenhouses, the closure phases constructed from Sentinel-1 acquisitions consistently exhibit positive signatures. The evolution of these observations appears to be related to the phenological stages of plants, as evidenced by crop calendars. Moreover, the signatures of closure phases stand out as a potential indicator of vegetation development under dense vegetation conditions when compared to coherence and normalized radar cross-section (NRCS). Two existing models, one based on dielectric variation in the sub-surface and another on volume scattering combined with perpendicular baselines, do not explain observed time series. Therefore, the presence of these positive closure phases implies the existence of supplementary factors contributing to closure phases associated with plant development. In this context, we explore two potential factors: variations in dielectric properties within crop canopies and the line-of-sight motion of crops. These factors are considered to establish connections between temporal changes in vegetation parameters and observed closure phase signatures. Regarding the first factor, we characterize the crop canopies using the dielectric constant of an equivalent medium, thereby capturing changes in wave propagation within the canopies due to leaves and vertical stalks development throughout the crop growth stages. We then model their contributions to closure phases in a manner analogous to an existing soil-moisture model. By using realistic vegetation parameters derived from in-situ measurements, this forward model generates synthetic data comparable in magnitude to the observations. As for the second factor, we propose an additional contributing mechanism to closure phases — skewed motion in the radar line-of-sight (LoS) direction induced by plant growth. This motion model is mathematically verified under a small-motion approximation. Both models offer valuable insights into the origins of geophysical closure phases.

Index Terms—Closure phases, plant development, propagation model, skewed-motion model.

I. INTRODUCTION

CLOSURE phases are defined as the sum of the phases of the three spatially averaged interferograms formed by circularly interfering three Synthetic Aperture Radar (SAR) images. Recent research has shown that there is a geophysical signal in these SAR interferometry (InSAR) closure phases [1]–[7]. In current literature, changes in dielectric properties of a medium including soil moisture variations, water content variations in vegetation and snow metamorphism, volume scattering in combination with perpendicular baselines, and differential movements are recognized as three contributors to geophysical closure phases [1], [5], [7]. Two analytical expressions have been developed to model closure phases induced by the first two mechanisms: a soil moisture dielectric

propagation model and a volumetric scattering model [1], [2]. Current research mainly focuses on the relation with soil moisture changes, while other physical processes in closure phases remain largely unexplored [2], [3], [5]–[9]. For example, the soil moisture model has been broadly used to retrieve soil moisture from radar stacks or to support the analysis of InSAR deformation time series. However, in the presence of vegetation, the validity of the soil moisture model is limited, as the vegetation development introduces additional components to closure phases which the soil moisture variation mechanism is not able to describe completely [3], [5], [7], [8].

Significant consistently positive closure phases are observed in Sentinel-1 interferometric time series during crop growth in the South of Spain. This signature is evident in agricultural areas, including open crop fields and greenhouses. Open crop fields, characterized by their exposure to stronger environmental forces, present a more complex scenario compared to greenhouses. The province of Almería, on the southeastern coast of Spain, has a dense concentration of greenhouses. While the plastic greenhouses add elements of complexity to the observed radar signals, they also provide a more controlled crop-growth environment. For example, we may expect smaller fluctuations in soil moisture, which should help isolate closure-phase contributions associated with the evolution of the crops. However, despite the differences in environmental conditions, the closure phases observed in corn and citrus fields exhibit similar signatures to those observed in greenhouses. As the crop-growth season varies from greenhouses to open fields, periods of positive closure phases appear at different times of the year. The existing soil moisture model, which considers soil moisture variations only [2], and the interferometric model for volumetric scattering, which is a function of scattering profile and perpendicular baselines [1], fail to explain the observed closure phase temporal signatures, in particular their positive bias. Therefore, the observed positive-signed signatures suggest the existence of one or several additional mechanisms leading to non-zero closure phases.

This paper explores the link between vegetation growth and closure phases. The remaining sections of the paper are structured as follows. Section II introduces the concept of closure phases and provides a summary of existing geophysical models to explain non-zero closure phases. In Section III, we describe the data used and the methodology applied in data processing. In Section IV, we provide empirical evidence for the existence of crop-growth-related closure phases with Sentinel-1 data examples over various agricultural areas and qualitatively analyze the closure phase signatures. Then, Section V predicts the plant contributions to closure phases. First, we distinguish observed closure phase signatures from signatures that existing models predict. Next, we propose two distinct closure phase models that account for vegetation

Y. Yuan, M. Kleinherenbrink and P. López-Dekker are with the Department of Geoscience and Remote Sensing, Delft University of Technology, 2628 CD Delft, The Netherlands.

development by considering wave propagation within a lossy medium and the variation of travel distance in line-of-sight (LoS). We then evaluate their potential to explain observed signals correlated with plant growth. Lastly, Section VI provides conclusions to the work and gives recommendations for future research.

II. BACKGROUND

Single-Look Complex (SLC) SAR data can be written in the form of a set of phasors $i = Ae^{j\phi}$, where A is the amplitude and ϕ is the phase. After alignment of SLCs obtained from two acquisitions, an interferogram can be computed as

$$\begin{aligned} I_{12} &= i_1 i_2^* \\ &= A_1 A_2 e^{j(\phi_1 - \phi_2)} \\ &= |I_{12}| e^{j\phi_{12}}. \end{aligned} \quad (1)$$

By using all combinations of three acquisitions, three interferograms can be computed. A so-called closure phase is then computed as the product of the three circularly generated interferograms [10], i.e. the phase of

$$I_{12} I_{23} I_{31} = |I_{12}| |I_{23}| |I_{31}| e^{j(\phi_{12} + \phi_{23} + \phi_{31})}, \quad (2)$$

such that

$$\Phi_{123} = \phi_{12} + \phi_{23} + \phi_{31}. \quad (3)$$

At single-look resolution, i.e. without any spatial averaging (*multilooking*) of the complex-valued interferograms, this quantity is always equal to zero by mathematical construction. However, when computing closure phases from spatially averaged (multilooked) interferograms, non-zero closure phases emerge. Under the assumption of spatial ergodicity, one can treat the multilooked interferogram as an estimate of its expected value. Besides decorrelation noise, non-zero closure phases emerge when we interfere data with contributions from different scatterer families, where each family exhibits distinct interferometric behaviors [1]. In current understanding, there are three potential geophysical origins of the non-zero closure phase: the first is the variations of dielectric properties within a medium, the second is volumetric scattering combined with perpendicular baselines, and the third is differential movements of objects [1] [5]. De Zan et al. developed two analytical expressions to interpret geophysical closure phases considering the first two mechanisms respectively [1], [2], [8]. However, a model for the third contributor has not been developed yet.

The first mechanism was studied by De Zan et al. for the specific case of non- and sparsely-vegetated areas, where variations in water content in the sub-surface change the dielectric properties of soil [2], [8]. This alteration in the wave propagation within the medium results in non-zero closure phases. The interferometric model for soil moisture is written as

$$I(\epsilon_{r1}, \epsilon_{r2}) = \frac{1}{2jk'_{z1} - 2jk'_{z2}}, \quad (4)$$

where k'_z is the complex-valued vertical wavenumber in the soil, and it is a function of the dielectric constant of the medium, denoted as ϵ_r [2]. This dielectric constant can be modeled based on soil moisture, soil texture, and frequency

[11]. Utilizing the interferometric model, the corresponding closure phase can be expressed as

$$\begin{aligned} \Phi_{123} &= \angle(I(\epsilon_{r1}, \epsilon_{r2})I(\epsilon_{r2}, \epsilon_{r3})I(\epsilon_{r3}, \epsilon_{r1})) \\ &= \angle\left(\frac{1}{2jk'_{z1} - 2jk'_{z2}} \frac{1}{2jk'_{z2} - 2jk'_{z3}} \frac{1}{2jk'_{z3} - 2jk'_{z1}}\right), \end{aligned} \quad (5)$$

where the \angle operation denotes extracting the phase of a complex value. This model was validated with in-situ soil moisture measurements [2] [8].

The second mechanism is revealed in scenarios where scatterers exist at different heights, exhibiting a skewed vertical scattering profile [1]. In such cases, non-zero closure phases emerge due to volume scattering in combination with perpendicular baselines. For a real-valued height-dependent scattering profile $f(z)$, this mechanism yields a closure phase

$$\begin{aligned} \Phi_{123} &= -\frac{1}{2}E[(z - \mu_z)^3]\kappa_{12}\kappa_{23}\kappa_{31} \\ &= -\frac{1}{2}E[(z - \mu_z)^3]\kappa_{123}, \end{aligned} \quad (6)$$

where $E[(z - \mu_z)^3]$ is the 3rd central moment of the scattering profile [1]. Each κ is the differential vertical wavenumber resulting from the perpendicular baseline B_\perp ,

$$\kappa = \frac{4\pi B_\perp}{\lambda R \sin \theta_i}, \quad (7)$$

where λ is the wavelength, R represents the one-way range of the secondary date and θ_i is the incident angle.

III. DATA PROCESSING

In this research, we use multiple datasets, including multilooked Sentinel-1 radar observables [12], a Sentinel-3 derived 300 m resolution Leaf Area Index product [13], *Sistema de Información Geográfica de Parcelas Agrícolas* (SIGPAC) shapefiles of land usage [14], daily precipitation data provided by Visual Crossing Corporation weather records [15], and the hourly ERA5 volumetric soil moisture product [16]. Except for the SIGPAC shapefiles, which correspond to 2017, the rest of the data stacks are from the time window 2016-12-10 to 2018-01-10 with different temporal and spatial resolutions (Table I). The data stack of Sentinel-1 images with 6 days of temporal sampling is our main data set for all fields. It includes two ascending passes with acquisition times around 18 o'clock, pass 1 and pass 74, which cover our area of interest (open crop regions and greenhouses area). The range of corresponding incident angles varies from area to area as shown in Table II.

Since large systematic geophysical closure phases often appear in low interferometric coherence scenarios, where the phase-noise level is high, the following two choices help expose the geophysical signals. First, closure phases are constructed using three successive acquisitions, which have the shortest temporal lag, to minimize additional coherence loss due to temporal decorrelation. In our consecutive Sentinel-1 acquisition scenario, each interval spans 6 days. Second, phase-noise suppression is achieved by substantial spatial averaging (multilooking).

TABLE I
INFORMATION FOR EACH DATASET.

Data set	Temporal resolution	Spatial resolution	Source
Multilooked Sentinel-1	6-day	1 km	European Union Copernicus programme
Sentinel-3 LAI	10-day	300 m	Copernicus Global Land Service
Land usage	1-year	-	Junta de Andalucía
Precipitation	1-day	-	Visual Crossing Corporation
ERA5 volumetric soil moisture	1-hour	9km	European Centre for Medium-Range Weather Forecasts (ECMWF)

TABLE II
SENTINEL-1 GEOMETRY INFORMATION FOR EACH FIELD.

Crop field	Sentinel-1 pass	Incident angle
Corn fields	Ascending pass 74	[34.02°, 38.83°]
Citrus fields	Ascending pass 74	[30.57°, 42.13°]
Greenhouses	Ascending pass 1	[37.77°, 43.82°]

In multilooking, we want all averaged samples to be re-realizations of the same random distribution. Therefore, we implement a three-step polygon-based multilooking strategy. We start with box-car multilooked $20\text{ m} \times 20\text{ m}$ resolution products instead of $5\text{ m} \times 20\text{ m}$ single-look complex (SLC) images to reduce computational costs. This small degree box-car multilooking process has a negligible effect on the final $1\text{ km} \times 1\text{ km}$ output. We refer to each multilooked data point, which represents the spatially averaged value of a set of single-look interferometric values, as a 'cell'. Then, we determine which $20\text{ m} \times 20\text{ m}$ cells fall within the polygons corresponding to a specific crop field type. This step utilizes SIGPAC geographic information, which offers polygons representing different land uses, along with the latitude and longitude coordinates of each $20\text{ m} \times 20\text{ m}$ cell. Lastly, to generate our $1\text{ km} \times 1\text{ km}$ product, we calculate the average intensities and interferograms over the selected $20\text{ m} \times 20\text{ m}$ cells within the $1\text{ km} \times 1\text{ km}$ window (see Appendix A for detail). For each crop field type, Figure 1 illustrates the multilooking processing steps.

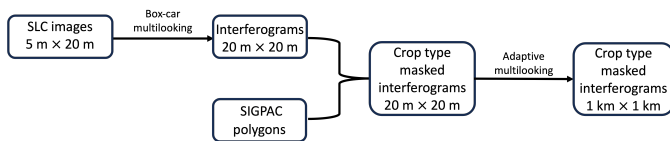


Fig. 1. Diagram of multilooking data progressing for each crop field type.

For each type of crop field, time series of a specific multilooked quantity behave differently due to differences in the equivalent number of looks (ENL) and other local conditions in each $1\text{ km} \times 1\text{ km}$ averaged cell. To reduce the risk of having a high noise-level time series, we exclude the $1\text{ km} \times 1\text{ km}$ cells with ENL smaller than one thousand. Despite differences in ENL and local conditions, we assume that time series of a specific multilooked product within fields of a given crop type share a common overall trend. We visualize the mean time series of each multilooked quantity, closure phases Φ_{123} ,

normalized radar cross-section (NRCS) σ and coherence γ , for three different classes, in Figure 5, 3, and 4, to show their evolution in time. In addition, we visualize the 5th and 95th percentiles of all closure phases time series to reveal the asymmetry in their distribution.

To support the qualitative analysis and interpretation of the observed closure phases, we provide two auxiliary data sets: Leaf Area Index (LAI) and precipitation records. As LAI characterizes vegetation canopies, we treat it as an indicator of crop growth and qualitatively study its correlation with closure phases for open crop fields. In addition, soil moisture variations have been recognized as one contributor to closure phases, and they are highly related to precipitation. Therefore, for each selected area, we include precipitation records from nearby areas to study the relation between precipitation events and radar observables.

IV. OBSERVATIONS

In southern Spain, several areas exhibit large positive one-year averaged closure phases, as shown in Figure 2. With Google map images and SIGPAC land usage information, we identified them as agricultural areas, including two open crop field areas and one greenhouses region. The open crop fields considered are corn fields (39°N , 6°W) around the town of Santa Amalia, and citrus fields (37.7°N , 5.5°W) in the upper Guadalquivir valley. The greenhouse area (36.7°N , 2.7°W) is located in the province of Almería where the greenhouse concentration is very high. For each class, the number of

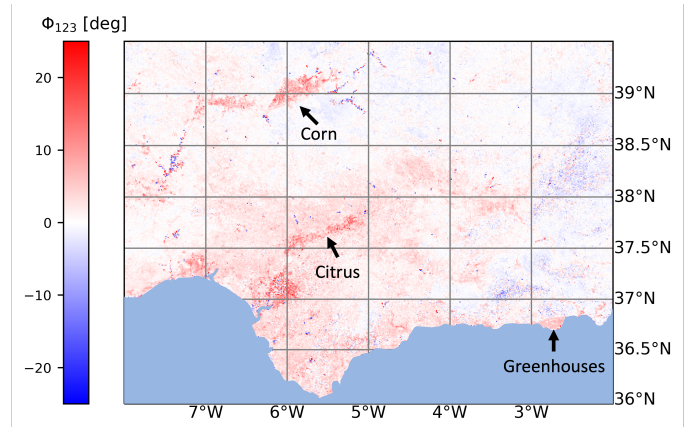


Fig. 2. VV polarized temporal mean closure phases over southern Spain in 2017

TABLE III
NUMBER OF AVERAGED 1 KM × 1 KM CELLS AND ENL INFORMATION FOR EACH FIELD.

Crop field	Cells	Mean ENL	Standard deviation of ENL
Corn fields	1187	$3.8 \cdot 10^3$	$1.3 \cdot 10^3$
Citrus fields	855	$2.3 \cdot 10^3$	$1.1 \cdot 10^3$
Greenhouses	563	$3.2 \cdot 10^3$	$1.4 \cdot 10^3$

averaged 1 km × 1 km cells and statistics of ENL are shown in Table III.

A. Observations over corn fields

Santa Amalia has a large portion of its surrounding fields allocated to corn production. Since SIGPAC does not have a class for corn, we first selected areas labeled as arable land, and then we selected polygons where LAI increases only during the corn crop-growth period from mid-spring to mid-autumn [17]. The mean radar observables time series represented in Figure 3 show a clear alignment with the LAI, in particular the peak of the mean closure phase, Φ_{123} . Within the time window where the LAI is larger than 0.5 m²/m², the distribution of closure phase time series indicated by their 5th and 95th percentiles shows a large spread from -10° to 55° as well as a significant asymmetry around the mean closure phase. The mean NRCS pattern, σ_l , seems to follow that of the LAI with a noisier signature except a 0.6 dB drop around mid-July. However, the mean coherence, γ , which drops significantly from 0.55 to 0.3 around April, increases steadily from late June until it reaches 0.55 again in October. Outside of summertime, the mean closure phase drops to 2.5° with variations between -2° and 5° except a local maximum around 12° in early March, while the mean coherence (between 0.2 and 0.7) and the mean NRCS (between -11.4 dB and -7.0 dB) both have large variations.

Corn in southern Spain is normally sowed around April. The emergence stage, about two weeks after sowing [18], coincides with a significant increase in the LAI from 0.25 m²/m² to 4.2 m²/m² as well as in the mean NRCS from -11.4 dB to -9.6 dB because of added scattering due to plants growth. As the crop at an early stage grows rapidly, such evolution causes high temporal decorrelation and thus brings the mean coherence down by 0.25. With the development of corn canopies, the LAI, the mean closure phase, and the mean NRCS start decreasing around August until the harvest season finishes and stalks are chopped, around October. However, as canopy conditions stabilize post-LAI peaks, the mean coherence starts increasing from 0.35 to 0.55. The occurrence of post-harvest chopping activities coincides with another 0.3 significant drop in the mean coherence in mid-October. After the corn growth period, fields enter a rest period with catch crops in fields until the next sowing season. In spring, a slight increase in LAI values around March may be associated with the growth of grass in fields, with the subsequent decrease attributed to mowing before planting.

Weather data from Santa Amalia shows frequent precipitation across the year. Such frequent precipitation events provide

an explanation for the large fluctuations in the mean coherence and the mean NRCS, while they are less obvious in the mean closure phase.

B. Observations over citrus fields

The Guadalquivir River basin hosts a large number of citrus fields. As shown in Figure 4, between spring and early winter, the mean closure phase again presents a consistently positive mean closure phase, Φ_{123} , with 90% of the distribution in the range 0° to 50° . These large positive closure phases are accompanied by reduced mean 6-day coherence values, which decrease from around 0.6 to around 0.3, and a relatively stable mean NRCS (-9.4 dB). Although the harvest season varies with species, most citrus are picked from mid-September till May [19]. This harvest period coincides with a decrease in the mean closure phase from 25° to near 0° . With this information, the increase in the mean closure phase from May can be explained by fruit growth and summer leaf flushes. Summer leaf flushes refer to new leaf growth, and they occur during the period of flowering and fruit development to maintain an adequate photosynthesis level in citrus trees [20].

In contrast to the corn fields, the LAI does not correlate with the radar observables in the citrus fields. There is a drop in the mean satellite-derived LAI values from 1.4 m²/m² to 0.8 m²/m², starting in May and ending before November. Considering citrus trees are evergreen and the plantation frame of citrus fields is about 6 to 7 m × 2.5 m [21], the limited above-ground biomass with wide space between trees makes grass at the ground relevant for the LAI. In the considered location, the hot temperatures ensure that grass usually dries in summer, which contributes to a decrease in LAI. Since LAI is highly affected by grass, the contribution from citrus canopies is hardly discernible in the LAI time series.

The weather record in Brenes (37.55°N, 5.87°W) indicates this area is very windy and has regular precipitation events outside of summertime. Large changes in the SAR-observables time series, especially in the mean coherence and the mean NRCS, are likely caused by these precipitation and gust events.

C. Observations over greenhouses

The time series of observables after averaging 1 km × 1 km cells with SIGPAC-designated greenhouses are visualized in Figure 5. The mean closure phase, Φ_{123} , is mainly positive across the year, with values ranging from 0° to 10° , and it drops close to zero (1°) during summer from July to September. The mean NRCS, σ_l , shows a similar trend with values as low as -8.8 dB during summer and as high as -7.2 dB out of the season. However, the mean coherence, γ , exhibits an opposite trend where it is significantly higher in summer (0.6) and lower during other seasons (0.4). The spread in the distribution of closure phases, indicated by their 5th and 95th percentiles, correlates with the coherence, the band is narrower when the coherence is higher and vice versa.

Collected field information from El Ejido greenhouses indicates that the majority of greenhouses are dedicated to the growth of everyday vegetables including pepper, cucumber,

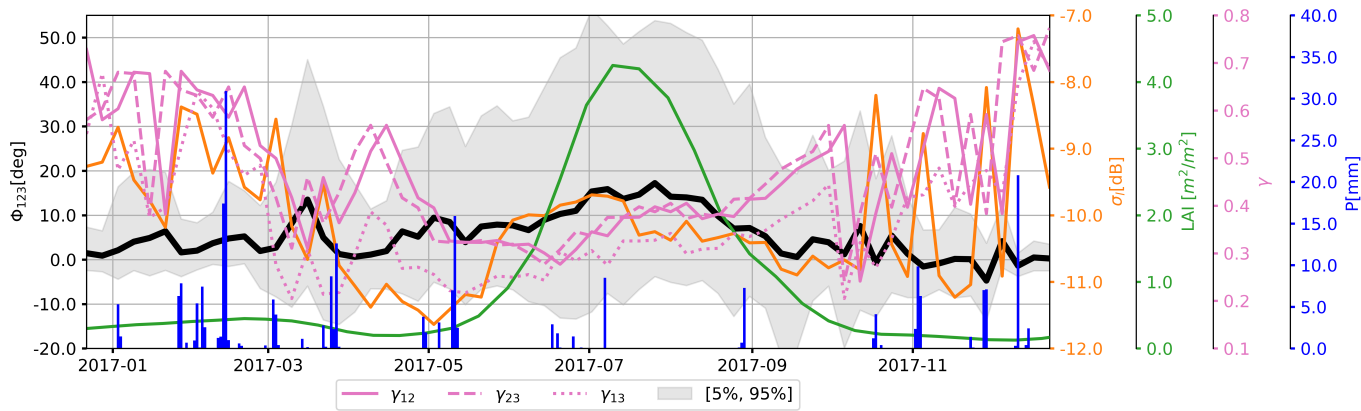


Fig. 3. Observations over corn fields around Santa Amalia: precipitation records P in Santa Amalia, mean time series of Leaf Area Index (LAI), VV polarized mean time series of closure phases Φ_{123} with corresponding 5th and 95th percentiles, NRCS σ_l and coherence γ .

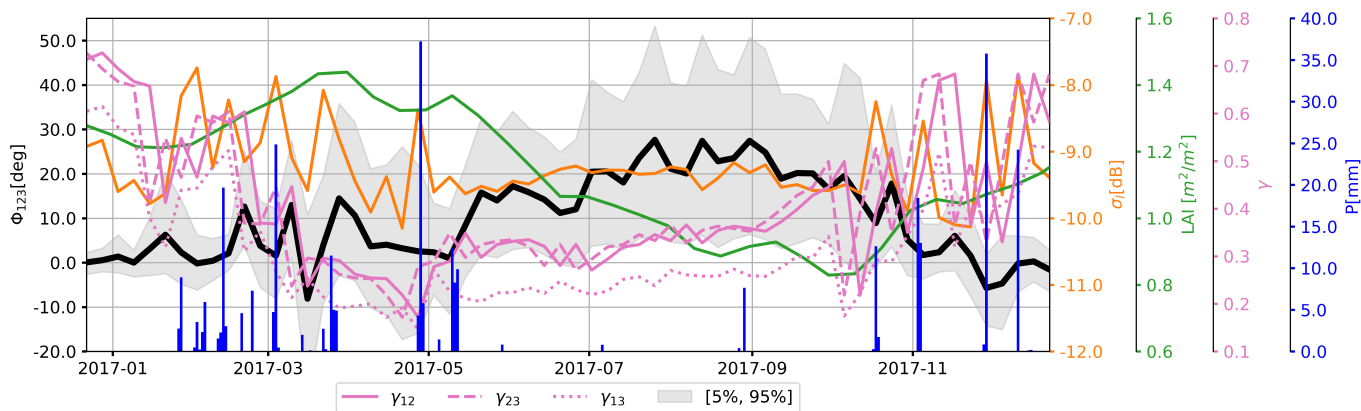


Fig. 4. Observations over citrus fields in upper Guadalquivir valley: precipitation records P in Brenes, mean time series of Leaf Area Index (LAI), VV polarized mean time series of closure phases Φ_{123} with corresponding 5th and 95th percentiles, NRCS σ_l and coherence γ .

tomato, and eggplant, and a small portion for fruits like melon and watermelon. According to local farmers¹, they typically plant vegetables at the end of August. This planting season coincides with the emergence of positive mean closure phase, increasing in the mean NRCS from -8.0 dB to -7.2 dB, and decreasing in the mean coherence from 0.5 to 0.3. The mean closure phase peaks in December with 10° when the harvest season starts. After that, there is a gradual decrease in the mean closure phase, while the mean NRCS and the mean coherence remain stable around -7.2 dB and 0.4, respectively. The mean closure phase remains positive until the end of June. From June, the mean coherence exhibits an increasing trend, while the mean NRCS shows a significant decreasing trend. These tendencies coincide with the end of harvest season for most crops. After harvesting, greenhouses typically undergo a period of rest and preparation for days to weeks.

¹We obtained this information by visiting thirteen different greenhouses in El Ejido and consulting with their owners. These greenhouses are situated across various locations around El Ejido: (36.74°N, 2.82°W), (36.78°N, 2.79°W), (36.77°N, 2.72°W) and (36.76°N, 2.71°W). Despite gathering field information from diverse locations, the information regarding growing season remains consistent. The authors would like to thank the owners of El Ejido greenhouses for providing field information to help us explain observed signals.

During the rest, only bare soil is left inside of greenhouses which explains the high mean coherence (0.6) and the lower mean NRCS (-8.8 dB) during summertime. Overall, a lower mean coherence, a higher mean NRCS, and a positive mean closure phase coincide with the crop growth period within the greenhouses.

Weather records in El Ejido show multiple precipitation events occurred throughout the year, especially outside of the summer season. Precipitation in spring and late autumn coincided with local minima in the mean coherence and the mean closure phase time series, followed by subsequent increases. Two events in October and November correlate with local peaks in the mean NRCS. Apparently, even though the plants are inside greenhouses, the return signal is affected by precipitation. One explanation could be water accumulation on plastic roofs.

D. Discussion

The nature of each radar observable determines its role in conveying information. The NRCS reflects the state of the observed object at the acquisition time. In contrast, the coherence and closure phases, formed with two and three acquisitions, respectively, provide information about the vari-

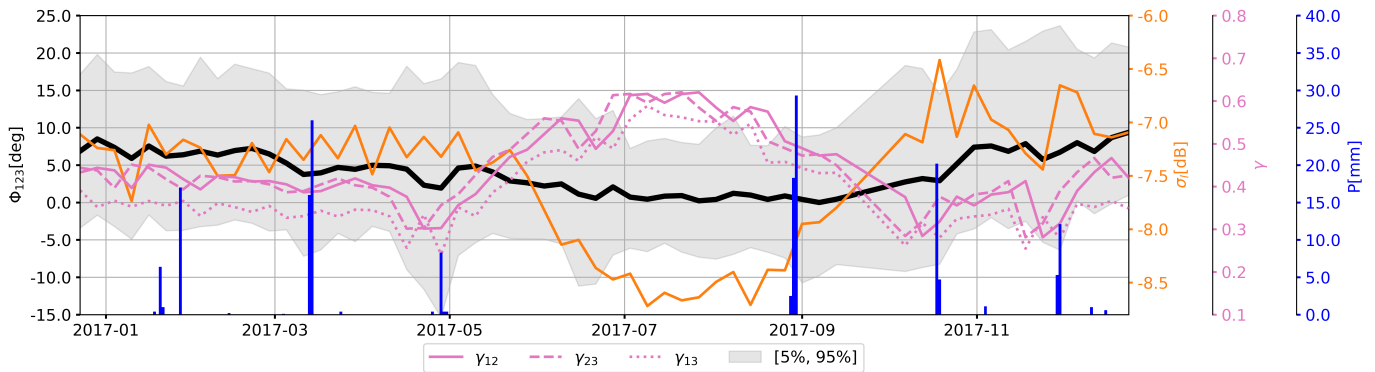


Fig. 5. Observations over Almería greenhouses: precipitation records P in El Ejido, VV polarized mean time series of closure phases Φ_{123} with corresponding 5th and 95th percentiles, NRCS σ_l and coherence γ .

ation in the state of the object over time. In conditions of dense vegetation, variations in radar observables highlight their varying sensitivity to detect changes in biomass.

Dense vegetation limits the C-band microwave penetration depth in the crop canopy, implying that the radar return corresponds primarily to vegetation and not to the underlying surface. This limited penetration also results in a relatively quick saturation of the NRCS time series, implying that the biophysical information content in the NRCS after this saturation is reached is limited. Although interferometric coherence is an indicator of change and has been studied as a vegetation index [22], it also tends to saturate at low values. Moreover, the magnitude of the coherence cannot be easily linked to a particular cause. All the observations discussed strongly suggest that the closure phase has the potential to serve as an indicator of plant growth or plant productivity. Although the signal is noisy, its mean varies smoothly during the crop-growth cycle, suggesting that a quantitative link may be established between the closure phase and the evolution of crop parameters.

V. MODELS: PROPOSAL AND VERIFICATION

Positive closure phase observations in agricultural areas indicate a relation to plant development. We try to interpret such signatures by modeling the contributions of different mechanisms to the closure phases. Starting with existing models, the soil moisture model and the interferometric model for volume scattering, we demonstrate that neither of these models produces positive closure phases that align with plant growth. Therefore, considering canopy developments only, we formulate and discuss two novel conceptual models that account for dielectric variations in canopies with vertical stalks and the motion of scatterers in line-of-sight direction during plant growth, respectively.

A. Existing soil moisture model

Since soil moisture data within the greenhouses is not available, we only study the soil moisture variation mechanism in open crop fields. Predicting the closure phases related to soil moisture changes consists of three steps. First, we interpolate hourly ERA5 volumetric soil moisture products in soil layers

0-7 cm with the acquisition time of radar observables (Figure 6 (a) and Figure 7 (a)). Second, we use the dielectric mixing model [11] in combination with Sentinel-1 frequency (5.405 GHz), ERA-5 volumetric soil moisture products, and soil texture in Seville, southern Spain (57.4% Sand and 19.6% Clay) [23] to model the dielectric constant of the soil. Third, we feed (5) with the modeled dielectric constant and predict the soil moisture-related closure phases. The simulations are compared with the observations in Figure 6 (b) and Figure 7 (b).

Results over both corn fields and citrus orchards show that most time of the year there is no correlation between closure phases induced by soil moisture variations and observed closure phases (Figure 6 and Figure 7). This lack of correlation is particularly evident during the corn crop growth period from April to October and the development period of citrus canopies from May to mid-September. The reliability

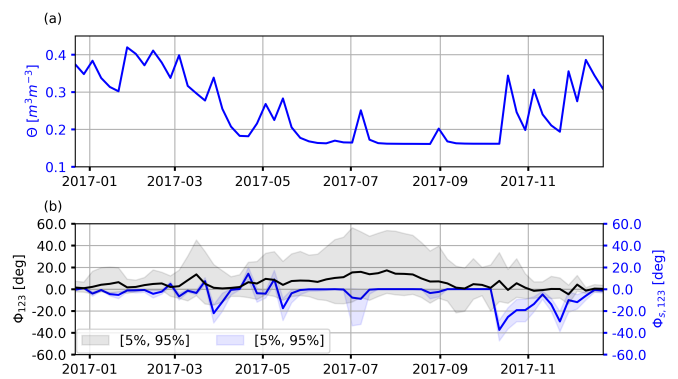


Fig. 6. Comparison between observed closure phases and closure phases modeled by the soil moisture model over corn fields: (a) mean ERA5 volumetric soil moisture products in soil layer 0-7 cm (blue) Θ , (b) closure phase observations Φ_{123} (black) and simulations $\Phi_{s,123}$ (blue) with corresponding 5th and 95th percentiles.

of the comparison may be affected by the heterogeneity in soil moisture variation that the 9 km resolution ERA5 product does not capture. However, the distribution of the modeled time series, as indicated by their 5% and 95% percentiles, suggests that soil moisture in these research areas exhibits limited spatial dynamics. Therefore, each ERA5 data point

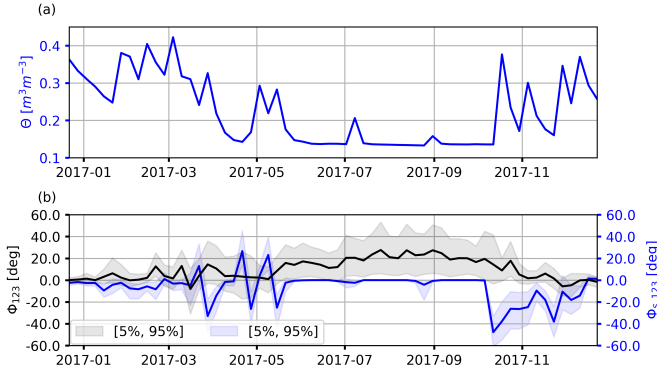


Fig. 7. Comparison between observed closure phases and closure phases modeled by the soil moisture model over citrus fields: (a) mean ERA5 volumetric soil moisture products in soil layer 0-7 cm (blue) Θ , (b) closure phase observations Φ_{123} (black) and simulations $\Phi_{s,123}$ (blue) with corresponding 5th and 95th percentiles.

represents soil moisture across a sizable area. Consequently, it can be deduced that, when vegetation significantly contributes to the scattered radar signal, the soil moisture model cannot explain the observed closure phases. Therefore, during the canopy development period under lush vegetation conditions, we can confidently discard soil moisture variation as being the main source of the observed signatures.

B. Existing interferometric model for volume scattering

Volume scattering in combination with perpendicular baselines is considered as one contributor to closure phases. We simulate its contribution using (6). As the scattering profile remains unknown lacking tomographic measurements, we only take the differential vertical wavenumbers κ as inputs to calculate closure phases resulting from this mechanism. The modeled time series in Figure 8 exhibit closure phases with fluctuation in signs over all fields. Since Sentinel-1 acquisitions over corn and citrus fields are from the same ascending pass, apart from negligible differences induced by variations in locations, the modeled closure phase time series show comparable behavior. In addition, as the contributions

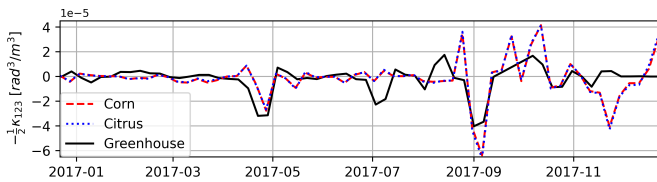


Fig. 8. Closure phase time series simulations from Sentinel-1 perpendicular baselines of ascending pass 1 (black solid line) and pass 74 (red and blue dotted lines).

from the triplets of vertical wavenumbers are very small (in the order of $1e - 5$), a large height difference within the product resolution would be required to cause closure phases with magnitudes in the same order as the observations. Therefore, the perpendicular baseline-related mechanism can also be excluded in explaining the observed consistent positive closure phases.

C. Equivalent-medium propagation model

Developments in crop canopies, including leaf and stalk growth, affect closure phase observations by altering the propagation of electromagnetic waves within the canopies. To establish a connection between observed closure phases and the evolution of crop parameters, we developed a propagation closure phase model for canopies with vertical stalks, excluding ground contribution. This propagation model is analogous to the existing soil moisture model [2], retaining the assumptions of isotropic and linear media. However, we substitute the dielectric constant of soil with that of the vegetation canopies and introduce a finite depth for the media based on plant height.

We assume the canopies are a dielectric mixture of stalks and leaves in the air, and describe it as a uniform equivalent lossy medium where stalks and leaves are represented by identical vertically oriented cylinders and randomly oriented thin circular discs [24]. A sketch in Figure 9 illustrates the wave propagation on the equivalent medium in a two-dimensional incidence plane xz . The interface between air and the canopies is parallel to the x -axis at $z = 0$. Modeling the

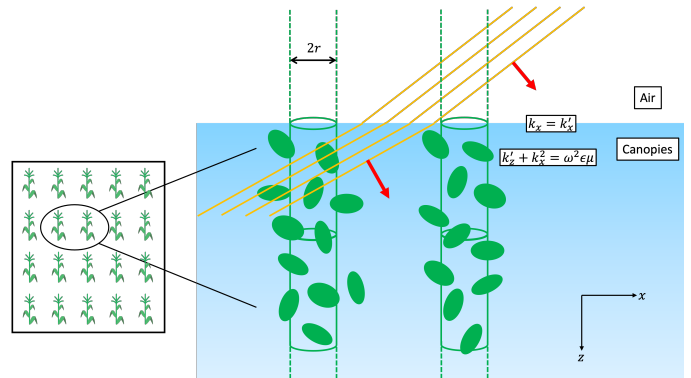


Fig. 9. Illustration of wave incidence and fraction on an equivalent medium model with a 2D geometry.

dielectric constant of the equivalent medium consists of three steps. First, we compute the dielectric constant of each element in canopies (leaf and stalk) with Ulaby and El-Rayes' linear model which takes frequency f_0 , salinity S , and gravimetric moisture m_g as inputs [25]. Second, we consider stalks in the air as a background dielectric medium. According to Ulaby et al., the dielectric constant of this background, ϵ_{rb} , relates to the complex refractive index n_p as,

$$\epsilon_{rb} = (n'_p + jn''_p)^2, \quad (8)$$

where n_p is a function of incident angle θ_i , radius of stalks r , dielectric constant of stalks ϵ_{rs} , and number of cylinders per unit area N [26]. Last, we add leaves, small in size relative to wavelength, to the background material, the dielectric constant of the full canopies can be written as

$$\epsilon_r = \epsilon_{rb} + \frac{v_l}{3} (\epsilon_{rl} - \epsilon_{rb}) \left(2 + \frac{\epsilon_{rb}}{\epsilon_{rl}} \right), \quad (9)$$

where v_l and ϵ_{rl} are the volume fraction and dielectric constant of leaves, respectively [24].

Taking the modeled dielectric constant of the equivalent medium as input, the expected value of an interferogram of two images with different dielectric constants can be written as

$$I(\epsilon_{r1}, \epsilon_{r2}) = \int_0^\infty f(z) e^{-j2k'_{z1}z} (e^{-j2k'_{z2}z})^* dz, \quad (10)$$

where $f(z)$ is the volumetric scattering coefficient which we assume to be constant, k'_{z1} and k'_{z2} are complex-valued vertical wavenumbers in canopies of each acquisition [2]. According to the wave equation, the vertical wavenumber within the equivalent medium is computed as

$$k'_z(\epsilon_r) = \sqrt{\omega^2 \epsilon \mu - k_x^2}, \quad (11)$$

where $\epsilon = \epsilon_r \epsilon_0$ is the permittivity of the medium, and $k_x = \frac{2\pi}{\lambda} \sin \theta_i$ is the horizontal wavenumber, which satisfies the boundary condition that $k'_x = k_x$. As we neglect the contribution from the ground and consider the vegetation canopies only in the model, the propagation of waves is limited by a finite depth of vegetation. In addition, since only the variations in the same group of scatterers contribute to the interferogram, we set the upper limit of the integral in (10) as the shorter plant height h between two acquisitions and rewrite the integral as

$$I(\epsilon_{r1}, \epsilon_{r2}) = \int_0^h f(z) e^{-j2k'_{z1}z} (e^{-j2k'_{z2}z})^* dz. \quad (12)$$

This integral gives

$$I(k'_{z1}, k'_{z2}, h) = \frac{1 - e^{-2jh(k'_{z1} - k'_{z2}^*)}}{2jk'_{z1} - 2jk'_{z2}^*}. \quad (13)$$

At the stage when the plant grows taller, the plant height h in (13) is the height at the earlier acquisition. Then the canopies' development-related closure phases can be computed as

$$\Phi_{123} = \angle \left(I(k'_{z1}, k'_{z2}, h_1) I(k'_{z2}, k'_{z3}, h_2) I(k'_{z3}, k'_{z1}, h_1) \right). \quad (14)$$

The flowchart in Figure 10 illustrates the input parameters we need and the steps we followed to derive the final equivalent-medium propagation model in (14).

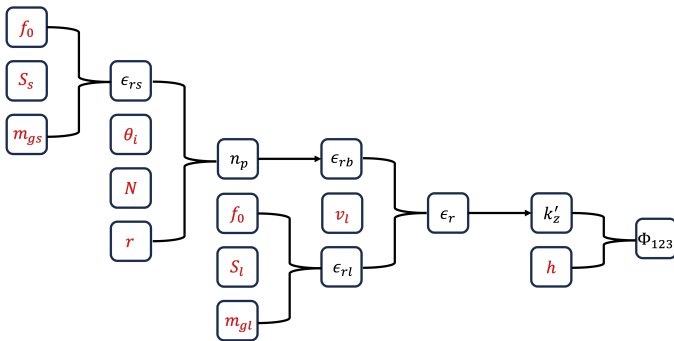


Fig. 10. Equivalent medium propagation model derivation flowchart with input parameters: frequency f_0 , incident angle θ_i , salinity of stalks S_s and leaves S_l , gravimetric moisture of stalks m_{gs} and leaves m_{gl} , number of cylinders per unit area N , volume fraction of leaves v_l , radius of stalks r , and plant height h .

We assume the crop type is the primary factor in affecting the evolution of vegetation parameters regardless of location. To qualitatively evaluate the outputs of our proposed model, we use in-situ measurements made in corn fields near Citra, Florida, USA in 2018 [27]. Vegetation parameters are measured in the cultivated field every 2 - 3 day, starting from the corn crops' planting on 13th April until their harvest on 18th June. Considering the revisit time of Sentinel-1, and discarding the first two weeks of measurements when the soil contribution is dominant as the ground is sparsely vegetated, we resample measurements to a 6-day sampling between 2nd May and 13th June. Following Ulaby et al. [28], with the measured vegetation water content (VWC) and dry biomass m_d , one can compute the gravimetric moisture m_g as

$$m_g = \frac{\text{VWC}}{\text{VWC} + m_d}. \quad (15)$$

The calculated values are visualized in Figure 11 (a). Using the

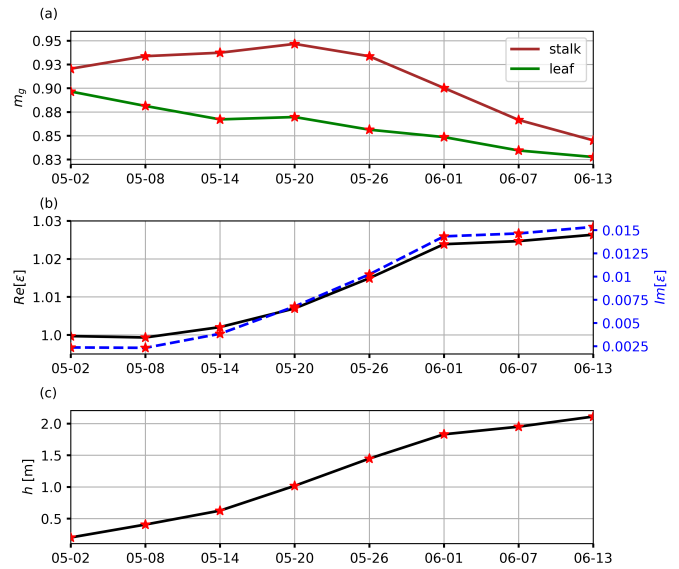


Fig. 11. Inputs and intermediate results of propagation closure phase model with red stars represent samples: (a) gravimetric moisture of stalk and leaf, (b) the dielectric constant of the equivalent medium which describe the full canopy condition, (c) measured plant height in corn crop fields near Citra, Florida, USA in 2018.

C-band frequency of Sentinel-1 $f_0 = 5.405$ GHz, an incident angle $\theta_i = 40^\circ$ and vegetation parameters, such as the stalk radius r , volume fraction of leaves v_l (approximated as 20% of stalk volume) and a constant salinity 10 psu for both stalk and leaf, we estimate the dielectric constant of full canopy ϵ_r with (9) (Figure 11 (b)). Taking the plant height as the last input (Figure 11 (c)), we can then model the corresponding closure phases.

The modeled closure phases in Figure 12, where the x-axis represents the first date of three acquisitions, exhibit positive values. Their magnitudes are comparable to observations in corn fields, particularly in May because the planting time in southern Spain is similar to that in the Florida research site. From the modeled results, we can infer the following: first, the rate of change in both the dielectric constant of the full

canopy and the plant height correlates to the magnitude of closure phases. This signature suggests the sensitivity of the model outputs to the first and the second derivative of the input parameters. Second, when the variations in the dielectric constant and the plant height are relatively small in June, the modeled closure phases drop to zero. However, observations still show positive closure phases. This disparity suggests we need a more complete and complex equivalent-medium propagation model.

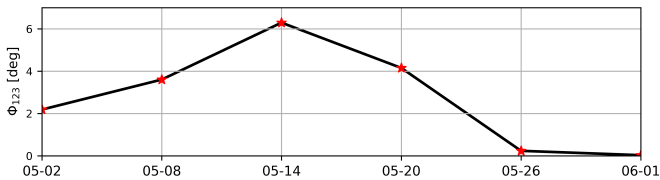


Fig. 12. Modeled closure phases with vegetation parameters in Figure 11 at C-band $f_0 = 5.405$ GHz and incident angle $\theta_i = 40^\circ$.

Our preliminary propagation model captures the propagation of the incident wave in the canopies under assumptions of an isotropic and linear equivalent medium with a finite depth and a uniform vertical scattering profile. The main value of the model is that, despite the oversimplifications made, it provides a biogeophysical explanation of the observed phase closures. It is clear that simplification of the canopy elements and the lack of other scattering contributions (e.g. surface and double bounce scattering) limit the predictive performance and applicability of the model.

D. Skewed motion model

Throughout the crop development, in addition to dielectric variations, plants exhibit growth in height from the emergence stage. Growth rates can be very high, as in the case of corn, where it is as high as 5 cm/day after emergence and gradually decreases after approximately two months (Figure 11 (c)) [29]. For other crops, such as citrus trees, growth rates are much slower. Crop growth will undoubtedly lead to decorrelation of the *scatterers*. However, we expect that some scattering centers will remain partially coherent as their position changes due to the growth process.

We consider a small magnitude of the LoS projection of velocity (in the order of 0.001 m/day) and develop a motion-induced closure phase model. The derivation of the model is largely analogous to the volumetric scattering model reflected in (6) (see Appendix B for detail), resulting in the skewed-motion model

$$\Phi_{123} = -8k_0^3 E[(v - \mu_v)^3] \tau^3, \quad (16)$$

where $k_0 = \frac{2\pi}{\lambda}$ is the radar wave number, $E[(v - \mu_v)^3]$ is the third order central moment of the velocity profile, and τ is the temporal lag in the case of closure-phase construction with continuous Sentinel-1 acquisitions. This model implies that under a small motion approximation, a skewed velocity distribution will lead to non-zero closure phases.

In the absence of ground truth measurements, we are currently unable to directly link the model to closure phase

observations. Nevertheless, under the assumption that some scatterers will remain coherent while being subjected to crop-growth-related motion, we can expect that a skewed motion distribution will introduce closure phases. On the one hand, as crops within a 1 km resolution cell exhibit diverse and non-uniform developmental characteristics, non-zero closure phases will manifest when there is a skewed distribution in their LoS motion. This phenomenon holds across different crop types. On the other hand, the level of skewness can be expected to vary with the stage of vegetation development, potentially resulting in closure phases that align with the crop growth cycle.

VI. CONCLUSION

Our work clearly points to the existence of a crop-development signature in closure phases and provides possible mechanisms to model it. Sentinel-1 observations show consistent positive closure phases throughout the plant development cycle in agricultural regions. The magnitude of these closure phases changes during the growth season, being clearly aligned with crop-growth rates. These observed closure phase signatures cannot be explained using existing models. To address this, we developed two new conceptual models, one based on variations in dielectric properties and the other on line-of-sight motion during vegetation development. These two new models provide plausible explanations for the observed positive closure phases.

We developed a propagation model under the assumptions of an isotropic and linear medium to account for the modifications in electromagnetic wave propagation caused by crop canopy developments. This equivalent-medium propagation model is able to relate temporal variations of biophysical parameters to closure phases and produce closure phases in comparable magnitudes as the ones observed in corn fields in southern Spain. While other crops may exhibit different behaviors, adjusting input parameters could allow for the adaption of this model based on corn canopies to other types of vegetation. Some disparities remain between modeled closure phases and observations in corn fields which indicate the incompleteness of the model. By constructing closure phases using acquisitions from different geometric passes, these observations have the potential to shed light on additional mechanisms and contribute to the advancement of the model.

The skewed-motion model established a connection between the distribution of the line-of-sight motion and closure phases within the framework of a small-motion approximation. Validation of the model is challenging without knowledge of the motion rate. While initially tailored for vegetation growth, this model holds relevance in scenarios featuring skewed slow motion, such as ice dynamics leading to a skewed deformation within a resolution cell. In instances where the velocity is large, fast-evolving parts of plants are less likely to contribute to closure phases due to decorrelation. Under such conditions, a tomographic experiment would help to investigate whether the observed closure phases originate from contributions near the ground.

There is an opportunity for future research to explore the development of a unified model that considers both sug-

gested mechanisms. Furthermore, in scenarios where radar can observe both soil and vegetation, a combination of soil and vegetation models would benefit the agricultural study. However, like many other related problems, such as modeling the NRCS of vegetation, physical models are always subject to oversimplifications that limit their performance. Their main value is that they provide a geophysical interpretation framework and that they expose sensitivities. For inversion purposes, parametric models are probably required.

We are not yet able to quantitatively exploit the full observed signal. On the one hand, Sentinel-1-derived closure phases in agricultural regions are inherently noisy, requiring us to work at relatively low product resolution, which also limits the scope of how the closure phases can be investigated and exploited. This will improve with future higher-resolution systems. On the other hand, further development of the model requires extensive ground-truth data and, possibly, dedicated experiments.

APPENDIX A

MATHEMATICAL REPRESENTATION OF MULTILOOKING

Multilooking is performed on both complex-valued interferograms and intensities. The multilooked intensities are calibrated to represent the NRCS values. Using the notation consistent with the main text, for a single pixel, we denote the amplitude as A , and the interferometric phase as $\phi_{12} = \phi_1 - \phi_2$. Correspondingly, the real and positive-valued coherence can be represented as $|\gamma_{12}|$. With these three quantities, we can construct the interferogram phasor as

$$I_{12} = |\gamma_{12}| A_1 A_2 e^{j(\phi_1 - \phi_2)}. \quad (17)$$

We then estimate the multilooked coherence as a sample average

$$\begin{aligned} \hat{\gamma}_{12} &= \frac{\sum_{i=1}^{N_p} I_{i,12}}{\sqrt{\sum_{i=1}^{N_p} I_{i,11}^2 \sum_{i=1}^{N_p} I_{i,22}^2}} \\ &= \frac{\sum_{i=1}^{N_p} \gamma_{i,12} A_{i,1} A_{i,2} e^{j(\phi_{i,1} - \phi_{i,2})}}{\sqrt{\sum_{i=1}^{N_p} A_{i,1}^2 \sum_{i=1}^{N_p} A_{i,2}^2}}. \end{aligned} \quad (18)$$

Here, N_p is the number of samples within a multilooking window. The multilooked interferometric phase is given by $\hat{\phi}_{12} = \angle(\hat{\gamma}_{12})$. In addition, the multilooked intensity is

$$\widehat{A^2} = \frac{\sum_{i=1}^{N_p} A_i^2}{N_p}. \quad (19)$$

APPENDIX B

SKewed MOTION MODEL DERIVATION

Let us start our derivation by writing a conceptual model of the received radar signal at time t as a summation of the reflection from a collection of scatterers

$$s(t) = \sum_{m=1}^{N_s} s_m(t), \quad (20)$$

where s_m represents complex signals from individual scatterers, N_s is the number of scatterers. For each scatterer, we

can write the reflected signal as a combination of phase and amplitude,

$$\begin{aligned} s_m(t) &= A_m(t) e^{j\phi_{0,m}(t)} e^{-2jk_0 r_m(t)} \\ &= s_{0,m}(t) e^{-2jk_0 r_m(t)}, \end{aligned} \quad (21)$$

where A_m is the amplitude of scatterers, $\phi_{0,m}$ is the phase of the scattering coefficient, $k_0 = \frac{2\pi}{\lambda}$ is the radar wave number, and r_m is the position of the scatterers in the line-of-sight direction. With another interferometric compatible acquisition at time $t + \tau$, we can construct the expected value of the interferogram, $I(\tau)$, as

$$\begin{aligned} I(\tau) &= E[s(t)s^*(t + \tau)] \\ &= E\left[\sum_{m=1}^{N_s} \sum_{n=1}^{N_s} s_m(t)s_n^*(t + \tau)\right] \\ &= \sum_{m=1}^{N_s} \sum_{n=1}^{N_s} E[s_m(t)s_n^*(t + \tau)] \\ &= \sum_{m=1}^{N_s} \sum_{n=1}^{N_s} E[s_{0,m}(t)s_{0,n}^*(t + \tau) e^{2jk_0(r_n(t+\tau) - r_m(t))}], \end{aligned} \quad (22)$$

where τ is the time lag. Assuming that the complex backscatter $s_{0,m}(t)$ and the term related to the position of the scatterer, $e^{-2jk_0 r_m(t)}$, are independent from each other, we can write $I(\tau)$ as

$$\begin{aligned} I(\tau) &= \sum_{m=1}^{N_s} \sum_{n=1}^{N_s} R_s(\tau) \delta_{mn} E[e^{2jk_0(r_n(t+\tau) - r_m(t))}] \\ &= N_s R_s(\tau) E[e^{2jk_0(r(t+\tau) - r(t))}] \\ &= N_s R_s(\tau) E[e^{2jk_0 \Delta r}], \end{aligned} \quad (23)$$

where $R_s(\tau)$ represents the autocorrelation of $s_0(t)$ between t and $t + \tau$, the Kronecker delta, δ_{mn} , reflects the assumption that the scattering coefficients $s_{0,m}$ are zero-mean independent identically distributed random variables, and $\Delta r = r(t + \tau) - r(t)$ is the differential motion of scatterers between two acquisitions.

To simplify the expected value of interferogram (23) in an integral form, we make three assumptions. First, we consider the LoS differential motion Δr as a function of velocity v and time lag τ ,

$$\Delta r = v\tau. \quad (24)$$

Second, we treat N_s as a scaling factor. Third, we assume the temporal decorrelation within the term $R_s(\tau)$ does not influence the closure phases. Focusing solely on the phase information, and normalizing the signal so that it has unit power, we define $I(\tau)$ as

$$\begin{aligned} I(\tau) &= \int f(\Delta r(\tau)) e^{2jk_0 \Delta r(\tau)} d\Delta r(\tau) \\ &= \int f(v) e^{j2k_0 v\tau} dv, \end{aligned} \quad (25)$$

where $f(\Delta r(\tau))$ is the probability density function (PDF) of the differential LoS motion, $f(v)$ is the PDF of the LoS velocity.

Following the same approach adopted by De Zan et al. [1], we equate (25) with the complex interferogram expression, $I(\tau) = A(\tau)e^{j\phi(\tau)}$. Then by taking the first to the fourth order derivatives for both sides, we derive the following relations:

$$\begin{aligned} A(0) &= 1 \\ \phi'(0) &= 2k_0\mu_v \\ A''(0) &= -4k_0^2E[(v - \mu_v)^2] \\ \phi'''(0) &= -8k_0^3E[(v - \mu_v)^3] \\ A^{IV}(0) &= 16k_0^4E[(v - \mu_v)^4]. \end{aligned} \quad (26)$$

To construct an approximation for closure phases, we expand each interferometric phase up to the fourth-order Taylor series with relations in (26). Since $\phi''(0) = 0$ and $\phi^{IV}(0) = 0$, by summing three interferometric phases in a circular way, we get

$$\begin{aligned} \Phi_{123} &= \phi_{12} + \phi_{23} + \phi_{31} \\ &\approx \phi'(0)(\tau_{12} + \tau_{23} + \tau_{31}) + \frac{1}{6}\phi'''(0)(\tau_{12}^3 + \tau_{23}^3 + \tau_{31}^3) \\ &= 2k_0\mu_v(\tau_{12} + \tau_{23} + \tau_{31}) \\ &\quad - \frac{4}{3}k_0^3E[(v - \mu_v)^3](\tau_{12}^3 + \tau_{23}^3 + \tau_{31}^3), \end{aligned} \quad (27)$$

where $E[(v - \mu_v)^3]$ is the third order central moment of the velocity profile. In the case of closure-phase construction with continuous Sentinel-1 acquisitions, $\tau_{12} + \tau_{23} + \tau_{31} = 0$ and $-\tau_{12} = -\tau_{23} = \frac{1}{2}\tau_{31} = \tau$. Therefore, (27) becomes

$$\Phi_{123} = -8k_0^3E[(v - \mu_v)^3]\tau^3. \quad (28)$$

We employed a simple approach by assuming a skewed-normal distribution for LoS velocity to generate closure phases with numerical simulations. According to the maximum likelihood estimation, the skewness γ_1 of a skewed-normal distribution can be written as a function of shape parameter α_1 ,

$$\gamma_1 = \frac{4 - \pi}{2} \frac{(\delta\sqrt{2/\pi})^3}{(1 - 2\delta^2/\pi)^2}, \quad (29)$$

where $\delta = \frac{\alpha_1}{\sqrt{1+\alpha_1^2}}$. When $\alpha_1 = 0$, the skewness $\gamma_1 = 0$ and thus the distribution becomes a normal distribution. Assuming the shape parameter α_1 follows a uniform distribution within the range of -28 to 28 , corresponding to a theoretically derived skewness (29) in the range of -0.99 to 0.99 , and considering 6-day revisit time of Sentinel-1, we simulated closure phases using (28) for different skewness inputs. The closure phases results, range from -30° to 30° , are visualized against the estimated skewness from the shape parameter in Figure 13. These results confirm that as long as the velocity distribution is skewed, the motion in LoS will result in a non-zero closure phase. Additionally, a larger degree of skewness produces larger closure phases.

ACKNOWLEDGMENT

This work was funded by the User Support for Space Research program (grant reference ALWGO.2017.017) of the Dutch Research Council (NWO).

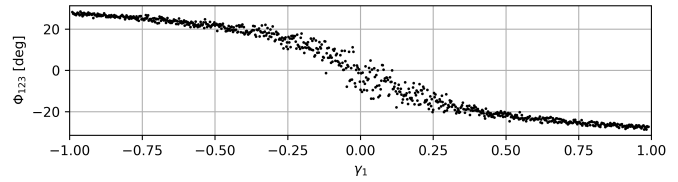


Fig. 13. Numerically simulated closure phases with the skewed motion model when the estimated skewness γ_1 ranges from -1 to 1 .

REFERENCES

- [1] F. De Zan, M. Zonno, and P. Lopez-Dekker, "Phase inconsistencies and multiple scattering in SAR interferometry," *IEEE Transactions on Geoscience and Remote Sensing*, vol. 53, no. 12, pp. 6608–6616, 2015.
- [2] F. De Zan, A. Parizzi, P. Prats-Iraola, and P. López-Dekker, "A SAR interferometric model for soil moisture," *IEEE Transactions on Geoscience and Remote Sensing*, vol. 52, no. 1, pp. 418–425, 2013.
- [3] Y. Eshqi Molan and Z. Lu, "Can InSAR coherence and closure phase be used to estimate soil moisture changes?" *Remote Sensing*, vol. 12, no. 9, p. 1511, 2020.
- [4] Y. Zheng, H. Fattahi, P. Agram, M. Simons, and P. Rosen, "On closure phase and systematic bias in multilooked SAR interferometry," *IEEE Transactions on Geoscience and Remote Sensing*, vol. 60, pp. 1–11, 2022.
- [5] S. Zwieback, X. Liu, S. Antonova, B. Heim, A. Bartsch, J. Boike, and I. Hajnsek, "A statistical test of phase closure to detect influences on DInSAR deformation estimates besides displacements and decorrelation noise: Two case studies in high-latitude regions," *IEEE Transactions on Geoscience and Remote Sensing*, vol. 54, no. 9, pp. 5588–5601, 2016.
- [6] S. Zwieback, S. Hensley, and I. Hajnsek, "Assessment of soil moisture effects on L-band radar interferometry," *Remote Sensing of Environment*, vol. 164, pp. 77–89, 2015.
- [7] F. De Zan, P. Saporta, and G. Gomba, "Spatiotemporal analysis of C-band interferometric phase anomalies over Sicily," in *EUSAR 2022: 14th European Conference on Synthetic Aperture Radar*. VDE, 2022, pp. 1–4.
- [8] F. De Zan and G. Gomba, "Vegetation and soil moisture inversion from SAR closure phases: First experiments and results," *Remote sensing of environment*, vol. 217, pp. 562–572, 2018.
- [9] S. Zwieback, S. Hensley, and I. Hajnsek, "A polarimetric first-order model of soil moisture effects on the DInSAR coherence," *Remote Sensing*, vol. 7, no. 6, pp. 7571–7596, 2015.
- [10] G. Perrin, F. Malbet, and J. Monnier, "Astrophysics with closure phases," *European Astronomical Society Publications Series*, vol. 6, pp. 213–213, 2003.
- [11] M. T. Hallikainen, F. T. Ulaby, M. C. Dobson, M. A. El-Rayes, and L.-K. Wu, "Microwave dielectric behavior of wet soil-part 1: Empirical models and experimental observations," *IEEE Transactions on Geoscience and Remote Sensing*, no. 1, pp. 25–34, 1985.
- [12] European Union Copernicus programme, "Copernicus Sentinel-1 data [2017]. Retrieved from ASF DAAC, processed by ESA," <https://search.asf.alaska.edu/>, Accessed on 27-05-2021.
- [13] Copernicus Global Land Service, "Leaf Area Index," <https://land.copernicus.eu/global/products/lai>, Accessed on 15-05-2023.
- [14] The Institute of Statistics and Cartography of Andalusia, "Sistema de Información Geográfica de Parcelas Agrícolas," <http://www.juntadeandalucia.es/institutodeestadisticaycartografia/sima/ficha.htm?mun=41902>, Accessed on 11-05-2023.
- [15] Visual Crossing, "Visual Crossing Weather," <https://www.visualcrossing.com/>, Accessed on 30-06-2023.
- [16] Muñoz Sabater, J. (2019), "ERA5-Land hourly data from 1950 to present. Copernicus Climate Change Service (C3S) Climate Data Store (CDS)," <https://cds.climate.copernicus.eu/cdsapp!/dataset/reanalysis-era5-land?tab=form>, Accessed on 15-02-2023.
- [17] U.S. Department of Agriculture, "USDA Foreign Agricultural Service," <https://fas.usda.gov/>, Accessed on 31-08-2023.
- [18] G. Clemente-Orta, R. Albajes, I. Batuecas, and M. Achon, "Planting period is the main factor for controlling maize rough dwarf disease," *Scientific reports*, vol. 11, no. 1, p. 977, 2021.
- [19] J. M. Ortiz, S. Zaragoza, and R. Bono, "The major citrus cultivars in Spain," *HortScience*, vol. 23, no. 4, pp. 691–693, 1988.

- [20] J. Syvertsen, M. Smith Jr, and J. Allen, "Growth rate and water relations of citrus leaf flushes," *Annals of botany*, vol. 47, no. 1, pp. 97–105, 1981.
- [21] C. Ortiz and A. Torregrosa, "Determining adequate vibration frequency, amplitude, and time for mechanical harvesting of fresh mandarins," *Transactions of the ASABE*, vol. 56, no. 1, pp. 15–22, 2013.
- [22] A. Villarroya-Carpio, J. M. Lopez-Sanchez, and M. E. Engdahl, "Sentinel-1 interferometric coherence as a vegetation index for agriculture," *Remote Sensing of Environment*, vol. 280, p. 113208, 2022.
- [23] F. López-Granados, M. Jurado-Expósito, S. Atenciano, A. García-Ferrer, M. Sánchez de la Orden, and L. García-Torres, "Spatial variability of agricultural soil parameters in southern Spain," *Plant and Soil*, vol. 246, pp. 97–105, 2002.
- [24] F. T. Ulaby, A. Tavakoli, and B. Thomas, "Microwave propagation constant for a vegetation canopy with vertical stalks," *IEEE transactions on geoscience and remote sensing*, no. 6, pp. 714–725, 1987.
- [25] F. T. Ulaby and M. A. El-Rayes, "Microwave dielectric spectrum of vegetation-part II: Dual-dispersion model," *IEEE Transactions on Geoscience and Remote Sensing*, no. 5, pp. 550–557, 1987.
- [26] F. T. Ulaby, D. Held, M. C. Donson, K. C. McDonald, and T. B. Senior, "Relating polarization phase difference of SAR signals to scene properties," *IEEE Transactions on Geoscience and Remote Sensing*, no. 1, pp. 83–92, 1987.
- [27] S. Khabbazan, S. Steele-Dunne, P. Vermunt, J. Judge, M. Vreugdenhil, and G. Gao, "The influence of surface canopy water on the relationship between L-band backscatter and biophysical variables in agricultural monitoring," *Remote Sensing of Environment*, vol. 268, p. 112789, 2022.
- [28] F. T. Ulaby and R. Jedlicka, "Microwave dielectric properties of plant materials," *IEEE Transactions on Geoscience and Remote Sensing*, no. 4, pp. 406–415, 1984.
- [29] M. M. Williams and J. L. Lindquist, "Influence of planting date and weed interference on sweet corn growth and development," *Agronomy Journal*, vol. 99, no. 4, pp. 1066–1072, 2007.



Paco López-Dekker Paco Lopez-Dekker (Senior Member, IEEE) was born in Nijmegen, The Netherlands, in 1972. He received the Ingeniero degree in telecommunication engineering from the Universitat Politècnica de Catalunya (UPC), Barcelona, Spain, in 1997, the M.S. degree in electrical and computer engineering from the University of California, Irvine, CA, USA, in 1998, under the Balsells Fellowship, and the Ph.D. degree in clear-air imaging radar systems to study the atmospheric boundary layer from the University of Massachusetts, Amherst, MA, USA, in 2003. In 2003, he joined Starlab Barcelona, where he worked on the development of GNSS-R sensors and techniques. From 2004 to 2006, he was a Visiting Professor with the Department of Telecommunications and Systems Engineering, Universitat Autònoma de Barcelona. In March 2006, he was awarded a Ramon y Cajal Grant to conduct pioneering research on bistatic synthetic aperture radar (SAR) at Remote Sensing Laboratory, UPC. Between November 2009 and August 2016, he led the SAR Missions Group at the Microwaves and Radar Institute, German Aerospace Center, Wessling, Germany. Since September 2016, he has been an Associate Professor with the Geoscience and Remote Sensing Department, Faculty of Civil Engineering and Geosciences. He has been deeply involved in the development of several radar missions and mission proposals, and is the Lead Investigator of the Harmony ESA Earth Explorer 10 Mission. He has coauthored over 50 peer-reviewed journal articles and more than 125 conference contributions in a broad range of topics related to radar remote sensing.



Yan Yuan Yan Yuan was born in Luding, China, in 1995. She obtained her bachelor's degree in geophysics from Ocean University of China, Qingdao, China in 2017. She received her master's degree in geoscience and remote sensing from Delft University of Technology, Delft, The Netherlands in 2020. During her master's study, she was involved in implementing forward models for the Earth Explorer 10 mission, Harmony. She is currently a doctoral candidate at the Faculty of Civil Engineering and Geoscience of Delft University of Technology, work-

ing on interferometric synthetic aperture radar (InSAR) closure phases.



Marcel Kleinherenbrink Marcel Kleinherenbrink obtained his master's degree at the faculty of Aerospace Engineering of Delft University of Technology, Delft, The Netherlands in 2013. He obtained his Ph.D. degree, on the observation of sea-level change and vertical land motion from space, at the faculty of Civil Engineering and Geoscience of Delft University of Technology in 2018. He specialises in the observation of the ocean surface using active radar instruments. In 2019 he became involved in the Earth Explorer 10 mission Harmony, for which

he implements forward models, investigates inversion strategies and provides performance estimates. Since 2018, he has been involved in numerous (ESA) projects related to future missions and novel retrieval algorithms for ocean observations.